REPORT DOCUMENTATION PAGE

Form Approved
OMB No. 0704-0188

Public reporting burden for this collection of information is estimated to average 1 hour per response, including the time for reviewing instructions, searching existing data sources, gathering and maintaining the data needed, and completing and reviewing this collection of information. Send comments regarding this burden estimate or any other aspect of this collection of information, including suggestions for reducing this burden to Department of Defense, Washington Headquarters Services, Directorate for Information Operations and Reports (0704-0188), 1215 Jefferson Davis Highway, Suite 1204, Arlington, VA 22202-4302. Respondents should be aware that notwithstanding any other provision of law, no person shall be subject to any penalty for failing to comply with a collection of information if it does not display a currently valid OMB control number. **PLEASE DO NOT RETURN YOUR FORM TO THE ABOVE ADDRESS.**

1. REPORT DATE (DD-MM-YYYY)	2. REPORT TYPE	3. DATES COVERED (From - To)
28-09-2007	Final technical report	15-05-2006 to 14-05-2007

4. TITLE AND SUBTITLE	5a. CONTRACT NUMBER
Characterization of iodine quenching and energy transfer rate constants for supersonic flow visualization applications	FA9550- 06-1-0369

5b. GRANT NUMBER

5c. PROGRAM ELEMENT NUMBER

6. AUTHOR(S)	5d. PROJECT NUMBER
Michael C. Heaven	

5e. TASK NUMBER

5f. WORK UNIT NUMBER

7. PERFORMING ORGANIZATION NAME(S) AND ADDRESS(ES)	8. PERFORMING ORGANIZATION REPORT NUMBER
Department of Chemistry, Emory University, Atlanta, GA 30322	

9. SPONSORING / MONITORING AGENCY NAME(S) AND ADDRESS(ES)	10. SPONSOR/MONITOR'S ACRONYM(S)
USAF/AFRL, NL AF Office of Scientific Research, 875 N. Randolph St, Room 3112, Arlington, VA 22203	

11. SPONSOR/MONITOR'S REPORT NUMBER(S)

12. DISTRIBUTION / AVAILABILITY STATEMENT

Unlimited — Distribution A: Approved for Public Release

13. SUPPLEMENTARY NOTES

14. ABSTRACT
Planar laser induced fluorescence (PLIF) imaging is being used to study the fluid dynamics of supersonic gas mixing in the nozzle from a chemical oxygen iodine laser (COIL). PLIF images are recorded using laser excitation of the I_2 B-X transition. Data for the temperature dependences of the $I_2(B)$ quenching rate constants are needed for the quantitative interpretation of the PLIF data. A Mach 2.6 supersonic nozzle system has been used in an investigation of the quenching of $I_2(B)$ by N_2, O_2 and He over the temperature range from 120 to 295 K. Quenching by both N_2 and O_2 exhibited a near linear dependences on temperature for T>150 K. Quenching by He was found to be unimportant under typical COIL operating conditions. The quenching rate constants have been used in a preliminary analysis of PLIF images.

15. SUBJECT TERMS
Chemical laser, energy transfer kinetics, flow visualization.

16. SECURITY CLASSIFICATION OF: Unclassified			17. LIMITATION OF ABSTRACT	18. NUMBER OF PAGES	19a. NAME OF RESPONSIBLE PERSON Michael C. Heaven
a. REPORT	b. ABSTRACT	c. THIS PAGE	unlimited	28	19b. TELEPHONE NUMBER (include area code) (404) 727 6617

Standard Form 298 (Rev. 8-98)
Prescribed by ANSI Std. Z39.18

20071015188

Final report for the project,

"Characterization of iodine quenching and energy transfer rate constants for supersonic flow visualization applications"

Grant # FA9550-06-⬛⬛⬛1 -0369

P.I.   Michael C. Heaven,
        Department of Chemistry, Emory University, Atlanta, GA 30322

Introduction

Two problems are encountered in designing nozzles for super-sonic I_2 injection in the chemical oxygen iodine laser (COIL). First, prediction of the mixing dynamics using computational fluid dynamics (CFD) methods is a challenging task. Madden has shown that high-level CFD models are needed to capture the complex turbulent flow characteristics. Secondly, uncertainties in the I_2 dissociation mechanism make prediction of the dissociation rate and the concomitant energy cost of dissociation difficult to assess. Validation of the CFD models for super-sonic injection is a critical task in the sequence that leads to the development of efficient super-sonic mixing nozzles. The group at AFRL (Kirtland AFB) is using planar laser induced fluorescence (PLIF) of the I_2 B-X transition to image the flow in a Mach 2.5 nozzle that is equipped with super-sonic injectors. The images observed in their current experiments show turbulent structures and poor penetration of the secondary flow (attributed to the shallow angle of injection). The raw PLIF images provide a qualitative picture of the I_2 spatial distribution. However, the I_2 excitation and relaxation kinetics must be taken into account in order to convert the images into quantitative concentration maps. The objective of the program described here was to investigate the quenching and energy transfer kinetics of $I_2(B)$ in a supersonic flow, and to develop kinetic models that can be used in the analysis of PLIF data.

Quenching cross-section measurements

a. Characterization of the nozzle

Quenching of $I_2(B)$ by N_2, O_2 and He over the temperature range from 295 to 150 K was investigated in a Mach 2.6 nozzle. The first task of this project was to configure the nozzle and verify that supersonic flow conditions had been achieved. Fig. 1 shows the nozzle assembly
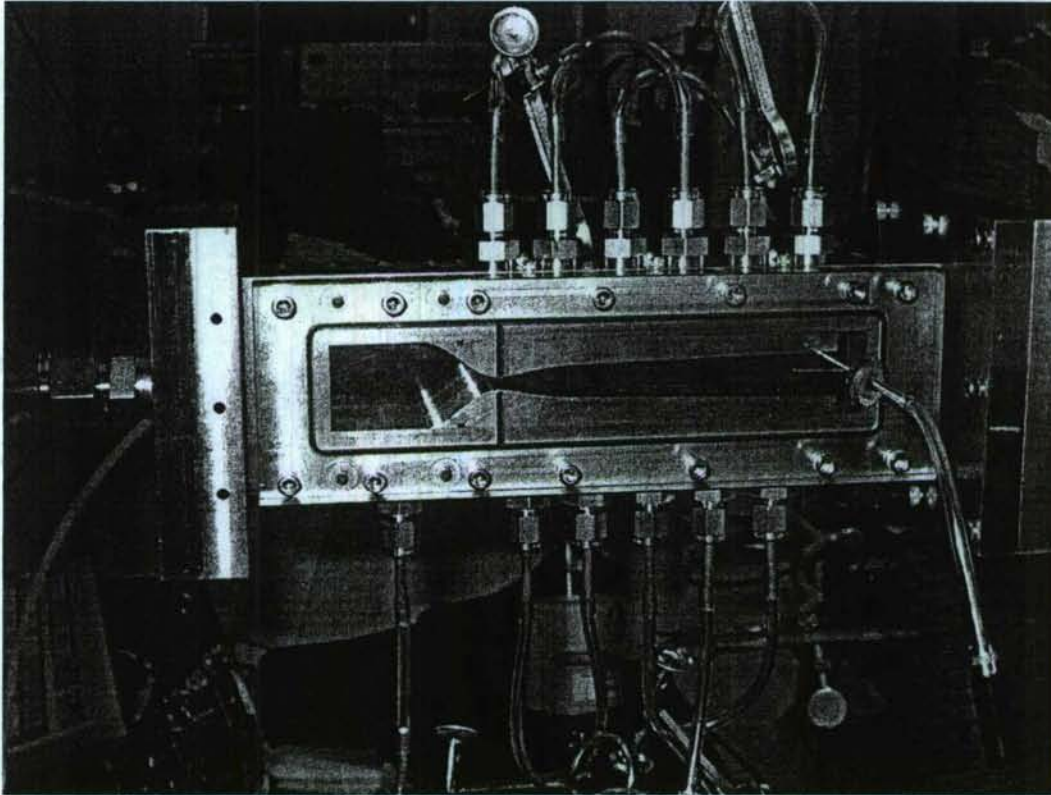

Fig 1. Photograph of nozzle assembly.

As can be seen in this picture, the nozzle was equipped with several ports to permit local pressure measurements. The port on the leftmost side of the picture, tapped into the bottom of the assembly, was used to measure the pressure in the plenum. The first port (leftmost) on the top of the nozzle accessed the transonic region of the flow. Eight other ports sampled the supersonic region of the flow. Lastly, the pressure tap mounted in the transparent side-wall of the nozzle assembly provided the Pitot pressure at the end of the expansion. The critical dimensions of the nozzle assembly are shown in Fig 2.
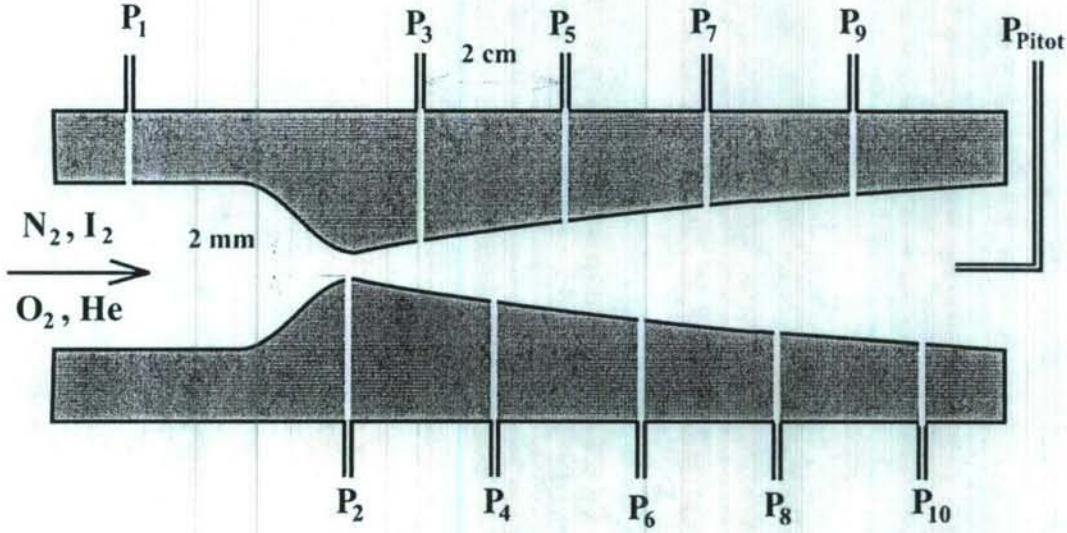
Fig. 2. Cross-section of the nozzle assembly. The pressure could be measured in the subsonic region (P_1), and in the transonic region (P_2) and at intervals of 1 cm along the flow (P_3-P_{10}). A Pitot tube was used to measure total pressure at the nozzle exit.

Supersonic operation of the nozzle was verified for flows of air, and the pure gases N_2, O_2 and He. A typical pressure profile for the nozzle operating with a mixture of I_2 (0.3 %) in N_2 is shown in Table 1 below

Table 1. Pressure distribution along the flow for N_2/I_2 mixture

P_1	P_2	P_3	P_4	P_5	P_6	P_7	P_8	P_9	P_{Pitot}
44	23.7	3.36	2.14	2.11	2.10	2.07	2.03	2.01	19.4

This profile was consistent with supersonic gas flow with a terminal Mach number of 2.66.

Local temperatures within the jet were determined using both the thermodynamic relationship

$$\frac{T_1}{T_n} = 1 + \frac{\gamma - 1}{2} M^2 = \left[\frac{P_1}{P_n} \right]^{\frac{\gamma-1}{\gamma}} \tag{1}$$

4

(where γ is the heat capacity ratio) and by fitting to the rotational line intensity distribution of the I_2 B-X spectrum recorded using laser excitation. Fig. 3 shows the experiment configured for laser induced fluorescence measurements.
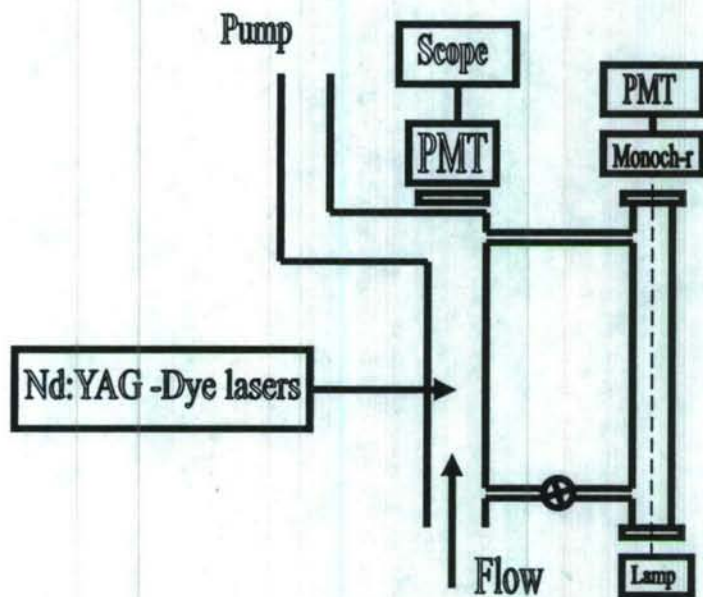

Fig. 3. Schematic view of the LIF measurement system.

Note that the small bypass cell shown on the right hand side of this figure was used to measure the concentration of I_2 in the flow using the B-X absorption band near 500 nm. The dye laser beam was directed along an axis perpendicular to the gas flow. Laser-excited fluorescence was detected by looking along the flow axis. The laser system used for these experiments consisted of a Nd/YAG pumped dye laser, operated at wavelengths near 577 nm. The linewidth of this laser, 0.06 cm^{-1}, was sufficiently narrow to permit rotational resolution of the B-X bands. Examples of rotationally resolved spectra recorded in the nozzle are shown in Fig. 4. Here the red trace was recorded with the laser positioned in the plenum, were the local temperature was that of the laboratory. The green trace was recorded with the laser positioned 6 cm downstream from the throat of the nozzle. Rotational temperatures were derived from these data using a spectral simulation program (c.f. Van Marter et al. *Chem. Phys. Lett.* 260, 201 (1996)). Overall, the agreement between the temperatures obtained from Eq. (1) and those obtained from
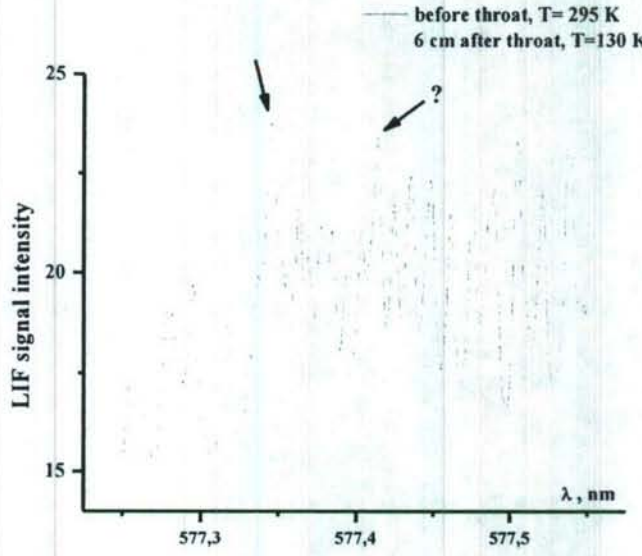
Fig. 4. LIF spectra obtained using N_2/I_2 with P_1= 50Torr, P_6= 3.7 Torr, P_{Pitot}=32 Torr and M=2.52.

the spectra was satisfactory (errors of no more than 10%). In several experiments we varied the conditions in the nozzle by adding a flow of air to the region downstream of the nozzle exit plane (which has the effect of decreasing the pumping speed). With this approach we could hold the pressure constant at a particular point in the flow and vary the local temperature by varying the plenum pressure and the pumping speed. To verify the proper operation of the nozzle under these conditions we compared the Mach number derived from Eq. 1 (denoted by M_{adiab}) with that obtained using the pressure measured by the Pitot tube (M_{Pitot}). The latter was obtained from the expression

$$\frac{P_{Pitot}}{P_n} = \left(\frac{\gamma+1}{2}\right)^{\frac{\gamma+1}{\gamma-1}} \left(\frac{2}{\gamma-1}\right)^{\frac{1}{\gamma-1}} \frac{M^{\left(\frac{2\gamma}{\gamma-1}\right)}}{\left(\frac{2\gamma}{\gamma-1}M^2-1\right)^{\frac{1}{\gamma-1}}} \qquad (2)$$

which, for γ=1.4, reduces to

6

$$\frac{P_{Pitot}}{P_n} = \frac{166.9M^7}{\left(7M^2 - 1\right)^{2.5}}$$

(3)

Table 2 shows a comparison of the Mach number at P_9 determined from Eq.'s 1 and 3. Here it can be seen that the agreement is good for high values of the Mach number (>2) but there are discrepancies for M in the range of 1.25-1.8. For this range we found that the Mach numbers derived from the Pitot tube pressure were more reliable.

Table 2. Mach numbers determined from Eq.'s 1 and 3 for P_9=2 Torr

P_1, Torr	P_{Pitot}, Torr	M_{Pitot}	M_{adiab}
43	18.8	2.63	2.65
37.6	18.5	2.62	2.56
32.8	17.1	2.51	2.48
27.4	15.6	2.4	2.36
22.5	12.95	2.16	2.24
20.2	12.7	2.15	2.17
16	9.4	1.82	2.02
12.6	6.75	1.5	1.86
10.6	5.2	1.25	1.75

(b) Measurement of quenching rate constants

Time-resolved fluorescence decay measurements were used to characterize the $I_2(B)$ quenching rate constants as a function of temperature. Fig. 5 shows typical time-resolved signals
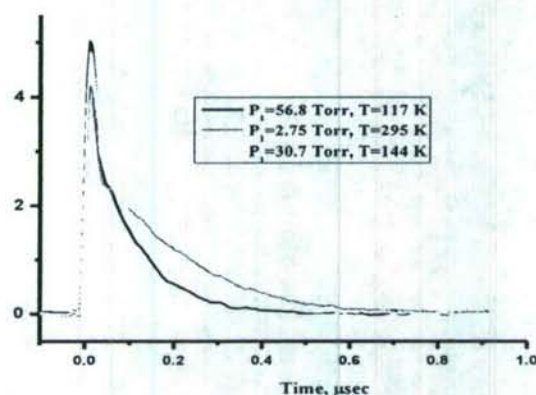

Fig. 5. $I_2(B,v=14)$ fluorescence signals for I_2/N_2 P_7=2.5 Torr

recorded for I_2 in N_2 with the probe laser positioned on the flow centerline, directly below the P_7 pressure tap. The quenching rate constant at each temperature was determined from the expression

$$\Gamma_{obs} = \Gamma_{sp} + k_q[q] \qquad (4)$$

where Γ_{obs} is the measured decay rate, Γ_{sp} is the spontaneous decay rate, k_q is the quenching rate constant, and $[q]$ is the number density for the quenching gas q. Fig. 6 shows a plot of the rate constant for quenching of $I_2(B, v=14)$ by N_2 over the temperature range from 110-295 K.
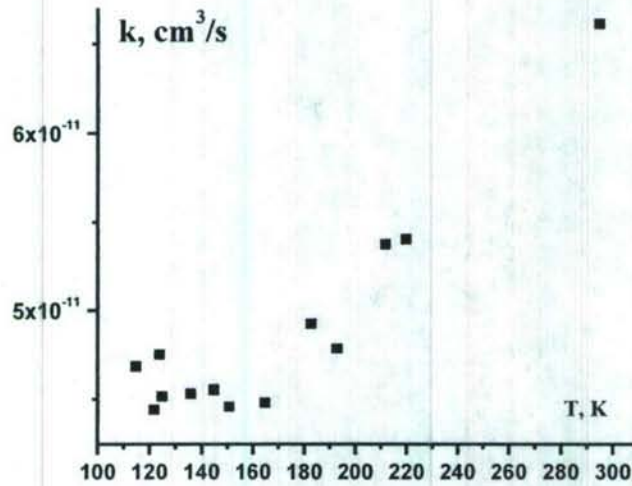

Fig. 6. Rate constant $k(T)$ for quenching of $I_2(B, v=14)$ by N_2

Over the range from 150 -295 K the rate constant is approximately linearly proportional to temperature, which indicates that the cross section for the quenching process increases slowly with decreasing temperature. In the region below 150 K the rate constant levels off at an approximately constant value. If this effect is real, it would indicate that the cross section was increasing more rapidly with decreasing temperature. This could be a consequence of the increasing importance long-range attractive forces at low temperatures. However, there was also some concern that the lowest temperature measurements were subject to systematic errors. For temperatures above 150 K the rate constant was well-represented by the expression ($cm^3\ s^{-1}$)

$$k_{N_2}(T) = (1.97 \pm 0.19) \times 10^{-11} + (1.59 \pm 0.09) \times 10^{-13} \times T$$

8

The temperature dependence of the rate constant for quenching of $I_2(B,v=14)$ by O_2 is shown in Fig. 7. Here again it can be seen that the rate constant has a near linear dependence on temperature for $T> 150$ K and, in this instance, the rate constant appears to increase with
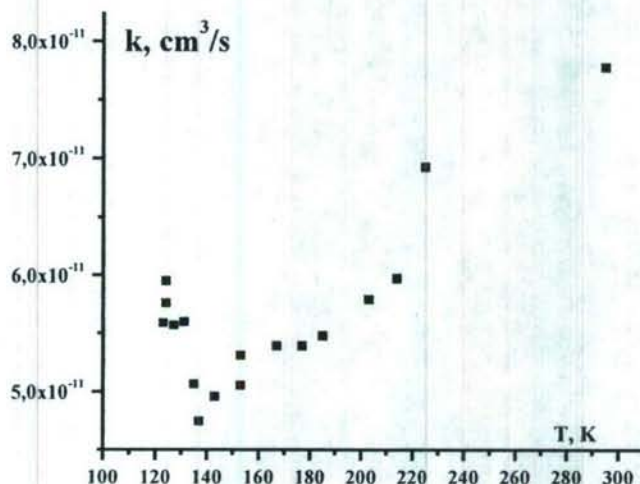

Fig. 7. Rate constant k(T) for quenching of $I_2(B, v=14)$ by O_2

decreasing temperature below 140 K. For $T>150$ K the rate constant is given by

$$k_{O_2}(T) = (2.18 \pm 036) \times 10^{-11} + (1.89 \pm 0.19) \times 10^{-13} \times T$$

Quenching of $I_2(B)$ by He was found to be very slow. Fig. 8 shows a decay curve recorded at a total He pressure of 3 Torr at $T \approx 160$ K. This fluorescence decay rate was close to that expected if the deactivation was determined by self quenching alone. Few measurement were done with pure He as the pumping speed was not sufficient to achieve stable supersonic operation of the nozzle. Since these measurements were carried out, new nozzle blades have been fabricated that define a contour that has a small throat size, and this will reduce the gas flow with He to a level that the current pumping system is able to cope with. Further measurements of the quenching rate constants using the small nozzle will be carried out in the next round of measurements.
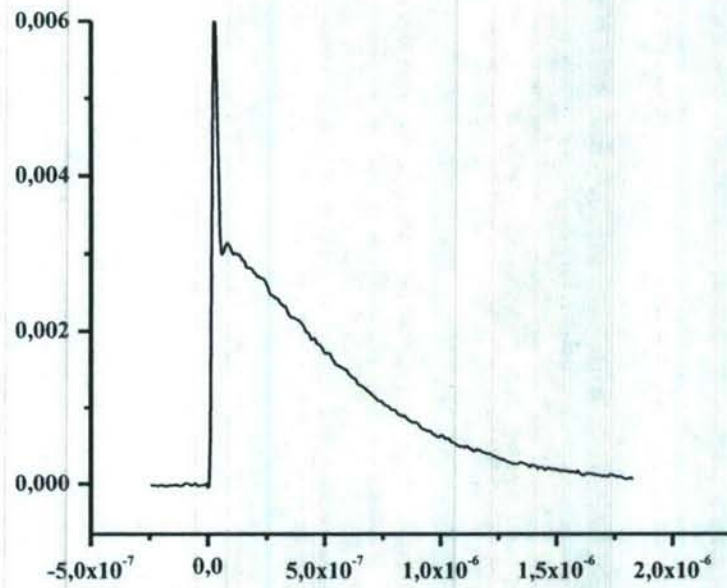
Fig. 8. Fluorescence decay $I_2(B)$ in a He supersonic flow at P=3 Torr.

Appendix. AIAA conference paper describing the initial kinetic model developed for analysis of I_2 PLIF images.

A Model for the Prediction of I_2 Fluorescence in the Presence of Pulsed Laser Radiation utilizing Computational Fluid Dynamic Simulation Datasets

Timothy J. Madden[*] and Carrie A. Noren
US Air Force Research Laboratory, Directed Energy Directorate
Kirtland AFB, NM 87117-5776

Luke Emmert
Department of Electrical and Computer Engineering, University of New Mexico, Albuquerque, NM, 87131

and Michael C. Heaven,
Department of Chemistry, Emory University, Atlanta, GA, 30322

[*] Senior Member, AIAA.

Introduction.

Imaging of fluid dynamic flowfields using non-intrusive diagnostics is a matter of practical interest to both experimentalists and theoreticians. All flow diagnostics such as Pitot tubes, hot-wire probes, pressure taps, particle image velocimetry, etc., offer the ability to obtain valuable information about the flow characteristics but perturb the local flow state to some degree. Evaluations must be made comparing the diagnostic need, the type of information provided, and the cost of the diagnostic among other considerations to determine the best choice. Non-intrusive diagnostics, particularly those using coherent radiation to generate a secondary radiative response from the particles in the gas, are attractive because of the inherent ability provide local measurements with minimal perturbation of the flow. In the case of chemical oxygen-iodine laser (COIL) flowfields, laser induced fluorescence (LIF) techniques are attractive for a variety of reasons, the non-intrusive nature of LIF, the ability to leverage existing COIL development infrastructure, the ability to get detailed localized information about flow structure, and the natural combination of LIF with the presence of I_2 in COIL flowfields, termed laser induced iodine fluorescence (LIIF). A drawback to the use of LIIF in COIL flowfields is the compressible nature of the flows, with large changes in pressure, temperature, and local species densities occurring within the field that must be accounted for in making quantitative interpretations of LIF generated imaging. The development of a model for the I_2 fluorescence that accounts for the thermodynamic variations while describing the spatial variation of photon production is useful from this standpoint as it allows for quantification of the compressibility effects from an interpretive standpoint while at the same time providing a tool for validation and verification of computational fluid dynamic (CFD) models.

LIF as a flow imaging technique originates in the work of Daily[1] Wrobel,[2] and Levy[3] who applied the non-intrusive nature of the technique as a convenient mechanism for imaging the development of flow structure for a variety of disparate flows including mixing layers, reacting flows, and expanding jets. Original work by Rapagnani and Davis[4] applied the technique as a flow diagnostic for the interrogation of the mixing systems in chemical lasers as a steady state flow diagnostic utilizing a cw laser source exciting the X→B transitions of I_2, although the issues associated with thermodynamic and quenching rate constant variation within the flow due to compressibility were not addressed. McDaniel[5,6] addressed the issue of use of LIIF as a quantitative, steady state diagnostic for compressible flows. His work found particular application in the mixing systems of high speed engines where the ability measure local quantities over small volumes was particularly useful for diagnosing mixing rates in these systems and creating multidimensional datasets for validation and verification of CFD models. The issue of LIF intensity variation resulting from compressibility effects was addressed by Fletcher[7] and Hartfield,[8] again for cw laser sources and steady state diagnosis. Given the analysis performed by McDaniel in developing the LIF for compressible flow application, the use of this model on CFD datasets was an attractive extension of the theoretical development. Hartfield performed such work, applying the model as a computational fluid imaging technique to steady state, 3-D CFD results and comparing directly to LIF imaging of high speed mixing system experiments. As mentioned earlier, LIF is an obvious candidate for application to COIL flowfields due to the use of I_2 as a reactant in these devices. Rapagnani and Davis[9] re-applied the technique for COIL flowfield imaging as a validation and verification tool complementing the 3-D CFD simulation efforts by Rapagnani.[10] Recent work by Noren[11,12] utilizing LIF of I_2 for the investigation of COIL mixing nozzles is coupled directly to this effort, and within this context the current effort represents a validation and verification study for the computational component.

The work performed in this investigation, while focusing on LIF, differs from the work of McDaniel, Fletcher, and Hartield in the use of short pulse laser pumping to excite the I_2 as opposed to the cw pumping sources utilized in that work. Thus the limiting assumptions and simplifications that result from the use of a cw laser source no longer apply, and the ordinary differential equations that describe the production and loss of the X and B states must be integrated directly over the period of the laser pulse to track photon production during the B→X excitation and reemission process. Additional differences regarding the temperature dependence of the quenching processes as well as the mechanisms that determine the populations of the vibrational-rotational states pumped by the laser pulse within the ground state manifold will be elucidated below.

Problem and Methodology.

The experiment that is modeled here is the planar LIIF, most commonly referred to as PLIF, interrogation of a Mach 3.4 He/I_2 jet injected into a He/O_2 flow that is expanding to Mach 2.2. The point of injection is just downstream of the primary flow nozzle throat on the upper surface. Figure 1. illustrates the experiment configuration consisting of the nozzle flow hardware, the laser sheet passing through the gas flow, and the CCD camera and Fig. 2 shows the secondary flow injector orifice as it was machined into the primary flow nozzle wall. The primary flow consists of 505 mmol/s He

and 125 mmol/s O_2 with a total pressure of 65 torr and a total temperature of 298.15 K. The secondary flow consists of 125 mmol/s He and 1 mmol/s I_2 with a total temperature of 425 K and a total pressure of 453 torr.

The PLIF pumping laser consists of a tunable dye laser using Rhodamine 6G dye pumped by a Nd:YAG. The measured wavelength of the tuned dye laser is 565.0947 nm and the measured bandwidth is 22.53 GHz. The pulse width for the dye laser output is 30 ns. The output beam of the dye laser is optically shaped to form a 600 μm thick sheet prior to transmission through the experiment for fluorescing the I_2. The light collection system uses a photo-intensified 512x512 pixel array CCD camera gated to 20 ns.

Relative to Fig. 1 the laser light can interrogate the gas at either 0° or 45° angles when the angle is measure with respect to an axis passing through the experiment parallel to the primary flow direction. The 0° interrogation is accomplished by passing the beam upstream through the gas parallel to the primary flow direction through a Lexan window downstream of the test section. The 45° interrogation is illustrated in Fig. 1, with the light passing upstream and across the flowfield with the 45° angle relative to the primary flow axis. The camera is positioned orthogonal to the laser light sheet for photon collection.

The approach taken for the development of a model for the PLIF imaging of the flowfield within the experiment is two-fold. The first part deals with the development and execution of a time dependent, 3-D, Navier-Stokes simulation for a LIIF experiment. The second part deals with the development and execution of a model for the physical processes underlying LIIF in this experiment. What is implicit here is the de-coupling of the physical model for the fluid dynamics from the physical model for LIIF. This approach is justified based upon the difference in time-scales for the pulsed LIIF and the fluid dynamics. The peak velocity in the primary flow direction within the experiment is order 1600 m/s. Over the course of the period during which photons are collected by the CCD, the camera gate of 20 ns, the flow in this peak velocity region will translate $3.2 \cdot 10^{-5}$ m. Given the length scale of the exit diameter of the jet of order 0.001 m, a representative length scale for the injected jet fluid, the flow translation distance of $3.2 \cdot 10^{-5}$ m represents 3.2% of this value. Practically speaking, the flow is frozen during the period of the camera gate and for this reason the model for the PLIF processes can be de-coupled from the CFD results.

The CFD model for the flow experiment utilizes a numerical solution of the Navier-Stokes continuity equations for mass, momentum, and energy, with individual mass continuity equations for each of the species. It is assumed that no chemical reactions occur within the gas during the experiment and formation of I_2-He, I_2-O_2, or I_2-I_2 van der Waals complexes is assumed negligible as well. Accurate description of the molecular diffusion of the species within the gas is important for the compressible, low Reynolds number conditions of these flows especially when considering the desire to compare the mixing of the secondary fluid as indicated by the PLIF model imaging of the CFD simulation to the PLIF images from the experiment. The Ramshaw-Dukowicz[13] approximation for multi-component diffusive transport is used including both gradient and pressure diffusion terms. The physical domain of the primary and secondary flows represented in Figs. 1 and 2 is represented in the computational domain of the simulation using a 13 block, 51.2 million cell grid shown in Fig. 3. The grid compression at the no-slip surfaces uses a minimum spacing at the wall set to $y^+ = 1$. The primary and secondary subsonic inflow boundaries for the simulation fix the total pressure and temperature while setting the second derivative of the static pressure to 0, allowing pressure waves to pass through while fixing the mass flux. The outflow boundary condition is a supersonic outflow and sets the second derivative of the dependent variables to zero. The solid surfaces are treated as no-slip boundaries with the temperatures of the lower nozzle surface and sidewalls set to a temperature of 298.15 K and the heated upper surface in which the He/I_2 orifice is located set to 400 K.

A consequence of the frozen flow approximation is that the inviscid and molecular transport aspects of the continuity relationships described by the Navier-Stokes equations become negligible and the only terms that remain significant are the time derivatives of the various upper and lower states in the I_2 X and B vibrational-rotational manifolds and the source terms that describe their production and loss. The physical processes that occur within the fluorescing process of I_2 can be organized as follows: the interaction of the laser light with the ground electronic state of I_2 such that a specific vibrational-rotational (v'',J'') state within the total manifold of X states is depopulated and a specific vibrational-rotational state (v',J') within the total manifold of the I_2 B electronic state is populated; through direct collisions and long range interactions with other molecules the ground v'',J'' state is re-populated and the v',J' excited state is de-populated; through spontaneous and simulated emission the entire manifold of populated B states is de-populated. Mathematically this is described as the set of coupled ordinary differential equations:

$$\frac{dX}{dt} = -\left(k_{in,X,He}He + k_{in,X,O_2}O_2\right)X + \left(k_{out,X',He}He + k_{out,X',O_2}O_2\right)X' + \Gamma_{rad}\left(B + \frac{B'}{2}\right)$$

$$\frac{dX'}{dt} = -\rho(v)\sigma_{abs}\left(X' - \frac{g_{X'}}{g_{B'}}B'\right) + \left(k_{in,X,He}He + k_{in,X,O_2}O_2\right)X - \left(k_{out,X',He}He + k_{out,X',O_2}O_2\right)X' + \Gamma_{rad}\frac{B'}{2}$$

$$\frac{dB}{dt} = -\left(k_{in,B,He}He + k_{in,B,O_2}O_2 + \Gamma_{rad} + \Gamma_{diss}\right)B + \left(k_{out,B',He}He + k_{out,B',O_2}O_2\right)B'$$

$$\frac{dB'}{dt} = \rho(v)\sigma_{abs}\left(X' - \frac{g_{X'}}{g_{B'}}B'\right) + \left(k_{in,B,He}He + k_{in,B,O_2}O_2\right)B - \left(k_{out,B',He}He + k_{out,B',O_2}O_2 + \Gamma_{rad} + \Gamma_{diss}\right)B'$$

[1]

In this set of equations, σ_{abs} is the absorption cross-section for the transition being pumped and $\rho(v)$ is the photon flux per unit area. $g_{X'}$ and $g_{B'}$ are the degeneracies for the ground and excited states respectively. X' is the population of the ground vibrational-rotational state that is pumped to the excited vibrational-rotational state B' within the B electronic state manifold. X is the sum total population of all the remaining vibrational-rotational states within the ground electronic state manifold and B is the sum total population of all the remaining vibrational-rotational states within the B electronic state manifold. $k_{in,X}$ is the total rate at which the X states are depopulated to fill X' during the pumping process through interactions with the He and O_2 molecules in the gas and as such is a rotational energy transfer rate constant. Similarly, $k_{in,B}$ is the total rate constant for the B states are collisionally depopulated to fill B'. Along these same lines, $k_{out,X}$ is the rate constant for population transfer from X' to the X states and $k_{out,B}$ is the rate constant for transfer from the B' state to the B states. Γ_{rad} is the radiative decay rate of the B' (and B') state. Γ_{diss} is the rate at which the B' state levels are lost through spontaneous (electronic predissociation) and collision induced dissociation processes. For the conditions of the experiments described here, Γ_{diss} is given by

$$\Gamma_{diss} = \Gamma_{sp} + k_{qHe}He + k_{qO_2}O_2 + k_{qI_2}I_2 \qquad [2]$$

where the $k_{q,M}$ terms are the rate constants for quenching by collision induced dissociation. Γ_{sp} is the decay rate for spontaneous predissociation. This results from the coupling of B state levels with a dissociative state that correlates with ground state atomic products. The states are coupled by rotational motion of the molecule, such that the predissociation rate is proportional to the rotational energy. The total decay rate for levels of the B state is then given by

$$\Gamma_{total} = \Gamma_{rad} + \Gamma_{diss} \qquad [3]$$

Values for the radiative and predissociative decay lifetimes (reciprocals of the decay rates) used here are shown in Table 2. In addition, Table 2 also lists the collision-free lifetimes (τ_0), which reflect the combination of radiative and predissociative decay.

Implicit within this model is the functional dependence on pressure and temperature, as many of the terms in these equations have some dependence on the two variables. The rate constants for rotational energy transfer, k_i, include temperature dependence and the product of k_iM includes both temperature and pressure through the number density. The I_2 dissociation rate is scaled by the temperature through the collision frequency of I_2 with itself, He, and O_2. The absorption cross section σ_{abs} is a weak function of pressure and temperature and the initial population of the ground vibrational-rotational state is a function of temperature through the Boltzmann population distribution. The temperature variation of the distributions for the odd-J levels within $v=0$ of the ground electronic state of I_2 is shown in Fig. 4, illustrating the wide variation of the equilibrium population distribution within the range of temperatures expected in the flowfield simulated here.

The temperature dependencies of the $I_2(B)$ quenching rate constants were examined by Azyazov and Heaven[14] in nozzle flow experiments using He and O_2 as the buffer gas. The use of the nozzle flow permitted temperature variation studies, and measurements were made between 150 K and 295 K. Over this range the rate constants exhibited a $T^{1/2}$ dependence. The results were consistent with Cappelle and Broida's[18] expression for the collisional part of Γ_{diss} in terms of temperature independent cross sections:

14

$$\Gamma_{diss} = \Gamma_{sp} + \sigma_{He}\left(\frac{8\pi}{\mu_{I_2,He}kT}\right)^{1/2}P_{He} + \sigma_{O_2}\left(\frac{8\pi}{\mu_{I_2,O_2}kT}\right)^{1/2}P_{O_2} + \sigma_{I_2}\left(\frac{16\pi}{m_{I_2}kT}\right)^{1/2}P_{I_2} \qquad [4]$$

with μ being the reduced mass for the collisions with I_2 and k being the Boltzmann constant. The collisional cross section for self-collisions, σ_{I_2}, is $70\cdot10^{-20}$ m^2, for collisions with He $\sigma_{He}=0.30\cdot10^{-20}$ m^2, and for O_2 $\sigma_{O_2}=5\cdot10^{-20}$ m^2.

Knowledge of the degeneracy of the individual states within the iodine molecule X and B manifolds was required for calculations of excitation rates and population distributions. For any rotational level of a diatomic rotor the degeneracy is $(2J+1)$ for the rotational angular momentum. Further degeneracy for I_2 is derived from the nuclear spin states of the molecule. The nuclear spin of ^{127}I is 5/2, so that the total spin quantum number for the molecule takes the values 0, 1, 2, 3, 4, and 5. Due to the restrictions imposed by nuclear exchange symmetry, the even nuclear spin states combine with even-J states while odd-spin states combine with odd-J for the ground state, which has *gerade* electronic exchange symmetry. Consequently, the total degeneracy is given by $g_X=3(6+(-1)^J)(2J+1)$. The symmetries are reversed for the B state as the electronic exchange symmetry is anti-symmetric. In this case the total degeneracy is given by $g_B=3(6-(-1)^J)(2J+1)$.

Rotational energy transfer rate constants were derived from the results of Lawrence et al.[19] Within the ground state, the room temperature rate constants for loss of X' in the presence of He and O_2 were $k_{out,X',He} = 4.7\cdot10^{-10}$ cm^3 molecule^{-1} s^{-1} and $k_{out,X',O_2} = 6.3\cdot10^{-10}$ cm^3 molecule^{-1} s^{-1}, respectively. Similarly for the B' state, $k_{out,B',He} = 5.5\cdot10^{-10}$ cm^3 molecule^{-1} s^{-1} and $k_{out,B',O_2} = 3.8\cdot10^{-10}$ cm^3 molecule^{-1} s^{-1}. Each of these rate constants was scaled by $(T/295)^{1/2}$ as discussed above. The rate constants for the transfer of population into the levels X' and B' from the surrounding rotational manifolds were then determined using the principle of detailed balance. For the X state the ratio was defined by the expression,

$$\frac{k_{in,X'M}}{k_{out,X'M}} = \left(\frac{3(6-(-1)^J)(2J+1)}{q_{rot,X}(T)}\right)\exp\left(\frac{-\bar{B}_{rot,X}J(J+1)}{kT}\right) \qquad [5]$$

and for the B rotational states,

$$\frac{k_{in,B'M}}{k_{out,B'M}} = \left(\frac{3(6+(-1)^J)(2J+1)}{q_{rot,B}(T)}\right)\exp\left(\frac{-\bar{B}_{rot,B}J(J+1)}{kT}\right) \qquad [6]$$

In these equations q_{rot} is the rotational partition function, J is the rotational quantum number for the X' or B' level, $\bar{B}_{rot}$ is the rotational energy constant and is 0.0373679 cm^{-1} ($7.42294\cdot10^{-25}$ J) for the X state and 0.0289937 cm^{-1} ($5.75944\cdot10^{-25}$ J) for the B state. The rotational partition functions for the X and B states, including nuclear spin weighting, are given by:

$$q_{rot,X}(T) = 3\sum_{J=0}^{200}(6-(-1)^J)(2J+1)\exp\left(\frac{-\bar{B}_{rot,X}J(J+1)}{kT}\right) \qquad [7]$$

and

$$q_{rot,B}(T) = 3\sum_{J=0}^{200}(6+(-1)^J)(2J+1)\exp\left(\frac{-\bar{B}_{rot,B}J(J+1)}{kT}\right) \qquad [8]$$

Truncation of the summations at $J=200$ was found to be a conservative approximation for temperatures below 300 K.

The absorption cross section σ_{abs} was calculated here as opposed to the use of measured values as the experiments determining those values were performed at atmospheric conditions whereas the pressures used here were 1 to 2 orders of magnitude smaller. The absorption cross section is related to the rate of excitation from the X' state, as given by the expression:

$$\frac{dX'}{dt} = -\left[\int_{-\infty}^{+\infty} B_{v',v''} \frac{I_v(v,t)}{c} g(v) dv\right] X'$$

[9]

$$= -\sigma_{abs} \rho(v,t) X'$$

where $g(v)$ is the Voigt lineshape function given by:

$$g(v) = \left[\left(\frac{a^2 4\ln 2}{\pi^3}\right)^{1/2} \frac{1}{\Delta v_D}\right]\int_{-\infty}^{+\infty} \frac{e^{-y^2}}{(\omega - y)^2 + a^2} dy$$

[10]

$$\omega = \frac{2\left(v - v_0\left(1 + \frac{V_i}{c}\right)\right)}{\Delta v_D}\sqrt{\ln 2}$$

[11]

$$a = \frac{\Delta v_L}{\Delta v_D}\sqrt{\ln 2}$$

[12]

$$y = \frac{2v_i v_0}{c\Delta v_D}\sqrt{\ln 2}$$

[13]

$$\Delta v_D = \frac{2}{\lambda}\sqrt{\frac{2RT\ell n2}{m_{I_2}}}$$

[14]

$$\Delta v_L = \frac{T_{ref}}{T^{1/2}} P \sum_{i=1}^{N} \alpha_i \chi_i$$

[15]

Δv_D and Δv_L are the Doppler and Lorentzian widths; v and v_0 are the frequency and line center frequency respectively; v_i is the molecular velocity of the molecule in the ith Cartesian coordinate direction; c is the speed of light; V_i is the bulk velocity component in the ith Cartesian coordinate direction; λ is the wavelength of the given transition; T is the temperature; R is the gas constant; m_{I_2} is the molecular mass of I_2; T_{ref} is the reference temperature for the pressure broadening coefficients; P is the pressure; and α_i and χ_i are the pressure broadening coefficient and mole fraction of the ith species upon the given transition. Following the work of McDaniel, the pressure broadening is taken to be 12 MHz/Torr for the bath at room temperature, $T_{ref} = 298.15$ K and this value is scaled by $T^{1/2}$. The laser pulse properties that determine $\rho(v,t)$ are known quantities measured during calibration of the laser source. The shape of the pulse is assumed to be Gaussian in both temporal and frequency space. The bandwidth of the pulse was measured to be 22.53 GHz and the energy of the pulse was $25 \cdot 10^{-3}$ J spread over 30 ns. The Einstein B coefficient for the transition in question, $B_{v',v''}$, is calculated using:

$$A_{v',v''} = \frac{|\langle\phi(v')|\phi(v'')\rangle|^2 v_{v',v''}^3}{\sum_v |\langle\phi(v')|\phi(v)\rangle|^2 v_{v',v}^3}\Gamma_{rad}$$

[16]

$$B_{v',v''} = \frac{A_{v',v''}}{8\pi h\lambda^3}\frac{g_{v',J'}}{g_{v'',J''}}$$

[17]

Where the squares of the vibrational overlap integrals, $|\langle\phi(v')|\phi(v'')\rangle|^2$ are the Franck-Condon factors and the transition dipole moment has been factored out using the R-centroid approximation. The Franck-Condon factors used here came from a database updated relative to the frequently cited work of Tellinghuisen[15]; the values for the particular transitions needed here are listed in Table 1. The values for the rates of radiative decay for the vibrational manifolds within the B→X transition needed here for determination the Einstein B coefficient were taken from the measurements of Broyer et al[16] and Vigué et al[17] and are listed in Table 2.

The ordinary differential equations [1] for the loss and production of the X, X', B, and B' states in the presence of the laser pulse are solved numerically using the DIVPAG solution routine from the IMSL library for each of the transitions listed in Table 1 within each cell of the CFD dataset. The resulting profile for the temporal development of

the B and B´ states for each of the pumped transitions can be used to determine the number of photons produced within each by integrating the product of the rate of radiative relaxation, Γ_{rad} and the total B state number density, over the period of the camera gate:

$$\int_{t_{gate}} \frac{d[photons]}{dt} dt = \int_{t_{gate}} \Gamma_{rad}(B(t) + B'(t)) dt$$

[18]

The total production of photons traveling within the solid angle defined by the light collection angle between the camera and the laser-illuminated sheet within the gas defines the predicted collection of photons by the CCD during the camera gate.

Results.

The 3-D Navier-Stokes simulation for the PLIF experiment nozzle hardware shown in Figs. 1 and 2 using the computational grid shown in Fig. 3 was executed to develop a prediction of the spatial, and if necessary, temporal variation of the flowfield. The model was executed with a timestep of $1\cdot10^{-8}$ sec for 100,000 time steps on the high resolution grid of 51.2 million grid cells after executing on lower resolution grids using $1/8^{th}$ and $1/64^{th}$ the number of grid cells. During the course of the execution of the simulation on each of these varying resolution grids, no evidence of flow fluctuation was encountered, and steady-state convergence of at least 2 orders of magnitude was obtained in each case. Fig. 5 illustrates the predicted structure of the jet as shown in an isosurface of constant I_2 mole fraction. Visible within this plot is the penetration and turn-over of the jet, as well as the outline of the counter-rotating vortex pair embedded within the jet structure. Fig. 6 shows the temperature distribution within a 2-D planar streamwise cut through the center of the jet. Evident within this perspective is the higher stagnation temperature of the secondary fluid with respect to the primary, 400 K versus 300 K, shown by the higher static temperature of the jet fluid for most of the duration of its' transit throughout the nozzle. These temperature variations are expected to impact the predicted variations in photon yield from the model for the fluorescence process.

The model for the I_2 fluorescence processes, as mentioned above, can be executed in a de-coupled manner from the CFD model due to the disparity in timescales between the two. Thus, the I_2 fluorescence model can be executed as a post-processor for the CFD dataset. Since the planar LIF sheets are much smaller than the total physical domain of the nozzle flowfield, a much smaller computational domain residing only within the PLIF sheet can be created as a subset of the larger domain of the CFD simulation. To accomplish this, grids 1 mm thick matching the overall size of the laser sheets were created and imported into the GASP software to interpolate from the CFD solution on the original grid to these '1 mm sheet' grids. After interpolation, the sheet grids with the quantities required for input to the I_2 fluorescence model including species densities and mole fractions, temperature, pressure, and cell volumes were exported and saved as separate datasets. The I_2 fluorescence model was then executed on these sheet datasets. The 600 μm thickness of the laser light is modeled within the equations for the photon flux by treating the profile as a spatial Gaussian profile with a full-width half-maximum of 600 μm. Fig. 7 illustrates the location of one of these grids used for illuminating a streamwise cut normal to the nozzle top wall through the center of the I_2/He injector orifice.

The basic set of principals underlying the model for the I_2 fluorescence process are that a local ground state population of I_2 is pumped to an excited state within the B electronic state manifold and through rotational relaxation the ground and excited state populations are enlarged and diminished during the course of the laser pumping process. Figs. 8 and 9 demonstrate the model prediction for the temporal response of the ground and excited states, X, X', B, and B' to the 30 ns laser pulse for a location within the He/I_2 jet. Fig. 8 shows the temporal variation of the B' variable representing the v', J' excited state, for each of the lines pumped. Transitions 7, 2, 4, and 6 are the strongest in terms of population, respectively, with the remaining lines being significantly weaker. The strength of these lines over the remaining lines is due to a combination of higher ground state populations and larger Einstein B coefficients. Fig. 9 shows the temporal variation of the X, X', B, and B' variables for Line 7 over the course of the laser pulse. The effect of the filling of the ground rotational state by the adjacent rotational states is apparent here as the X' population decreases by only 10% during the course of the pulse. However, the total population that is generated in the B and B' variables for the excited state is 20 times larger at the peak than that lost from the X', thus clearly illustrating the importance of the rotational energy transfer from the adjacent ground states in the generation of the excited states and in turn photons from fluorescence.

The radiative decay rate determines the photon flux from the excited states in the model. The total fluorescence decay lifetime (reciprocal of the decay rate defined by Eq. [3]), is measured in the PLIF experiment, providing an avenue for validation. Fig. 10 shows a comparison between a plot of the lifetime as measured in the PLIF experiment with that predicted by the fluorescence model within the PLIF sheet illustrated in Fig. 7. The lifetime values within the He/I_2 jet

were on the order of 50 ns with lengthening of the lifetime to order 100 ns further downstream as the collisional influence decreased due to decreasing temperature and pressure. Overall, the comparison between the experiment and model lifetime values is good, validating the quantitative and quantitative aspects of the lifetime calculation portion of the model.

Direct comparisons between PLIF images from the experiments and images generated using the I_2 fluorescence model are shown in Figs. 11-15. The model images were generated by summing the total photon yield in the direction orthogonal to the sheet, and dividing by the cross-sectional area of the cell faces parallel to the sheet to convert absolute photon counts into photon fluxes or effectively intensity. Fig. 11 shows the comparison within the sheet through the injector orifice parallel to the flow direction. The primary jet is clearly illuminated with the highest intensities in the image with a secondary structure associated with the counter-rotating vortex pair (CRVP) seen between the primary path of the jet fluid and the nozzle wall. In the model generated image, the region between the primary jet path and the structure associated with the CRVP is not illuminated as brightly as in the experiment image. This difference may be due to an inaccuracy of the model, or may be due to saturation effects within the experiment image that are not captured here. In all images shown here, the lightest or whitest grayscale shades are associated with the brightest fluorescence, and he maximum in the contouring scale is set to this value. However, in the experiment images, some pixels may have been saturated during the course of the light collection, and would not accurately register the highest fluorescence intensities, thus shifting the ratio of highest to lowest intensity recorded downward and shifting the grayscale contouring in the image. The end effect would be a brightening of lower intensity regions relative an image without saturation. As the saturation characteristics of the CCD camera used to collect the experiment images are not built into the I_2 fluorescence model, differences between the model and experiment images with some saturation will be found. Nonetheless, the comparison between the jet penetration and trajectories is very good between both images.

Figs. 12-15 show images from light collection in which the planar laser sheet interrogates the flowfield at a 45° angle with respect to the primary flow direction as illustrated in Fig. 1. Figs. 12 and 13 show comparisons between the experiment images at the trailing edge of the injector orifice with two separate images from the model. The first comparison in Fig. 12 uses a fluorescence model image in which the predicted number of photons generated during the laser pulse is integrally summed in the direction orthogonal to the sheet to mimic the effect of the finite sheet thickness of 600 μm. While both images show clear illumination of the edges of the fluid within CRVP, the model shows more illumination within the center region of the jet fluid. This difference could be due to a thinner sheet of fluid being illuminated within the experiment than the indicated sheet thickness of 600 μm, an important consideration when imaging structures having the same scale as the sheet thickness. Fig. 13 compares an image from the model using only a single plane at the center of the sheet instead of the integrally summed technique. The model prediction shows sharp resolution of the CRVP structure as do the original and the experiment images, but more fluid remains resolved within the CRVP than in the experiment. Thus, it is possible that slight differences in the location of the sheet between the experiment and the model could be contributing to the illumination of slightly different segments of the same fluid structure. Figs. 14 and 15 show comparisons further downstream, at locations 3 and 7 cm downstream of the injector orifice. The model images used the integral summing of the photon contributions through the thickness of the sheet, and very good agreement is demonstrated between the experiment and model images, clearly showing nearly identical structure of the CRVP and associated fluid within the jet. The model images are slightly darker than the experiment images as the grayscale contouring is fixed to that used in the injector imaging in Fig. 12, and tends to confirm the notion regarding the shift in the grayscale contouring in the experiment images due to saturation.

Summary and Conclusions.

In conclusion, the results show here demonstrated the development and application of a model for the fluorescence of I_2 in the presence of a pulsed laser source. Very good agreement between the model and the experiment PLIF images was found, but at the same time illustrated the challenges for comparing high resolution imagery and high resolution CFD simulations.

Future work will focus on detailed examinations of the quantification of CCD pixel saturation, precise quantification of the laser sheet positioning and width, and parameterizations of mixing studies.

Transition	v'', J''	v', J'	λ (nm)	$B_{v';v''}$ (s^{-1})	Degeneracy Ratio	FCF
1	1, 115	22, 116	565.083	$3.36 \cdot 10^{16}$	0.9915	0.0345
2	0, 29	18, 28	565.084	$9.70 \cdot 10^{15}$	1.0345	0.0116
3	0, 129	20, 130	565.0873	$1.64 \cdot 10^{16}$	0.9924	0.0168
4	1, 79	21, 80	565.0918	$3.52 \cdot 10^{16}$	0.9877	0.0366
5	0, 125	20, 124	565.0971	$1.61 \cdot 10^{16}$	1.0080	0.0168
6	0, 34	18, 35	565.0974	$1.03 \cdot 10^{16}$	0.9722	0.0116
7	1, 75	21, 74	565.0975	$3.43 \cdot 10^{16}$	1.0133	0.0116
8	0, 96	19, 97	565.0977	$1.33 \cdot 10^{16}$	0.9898	0.0142

Table 1. Data for the transitions used in the I_2 fluorescence model.

Transition	τ_{rad} (ns)	τ_{pred} (ns)	τ_0 (ns)
1	909.1	3055.3	700.6
2	970.9	94732.9	961.0
3	892.9	2366.5	648.3
4	909.1	6430.0	796.5
5	892.9	2600.1	664.6
6	970.9	61050.1	955.7
7	909.1	7507.5	810.9
8	917.4	5163.0	779.0

Table 2. Lifetime data used in the I_2 fluorescence model.
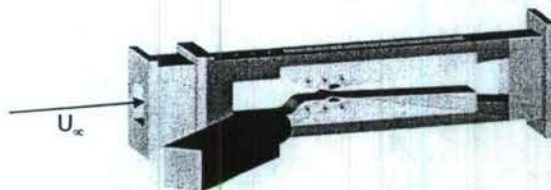
Figure 1. Representation of the PLIF experiment configuration simulated here. The laser sheet is passing through the experiment at a 45° angle and the camera is oriented orthogonally to the illuminated sheet.
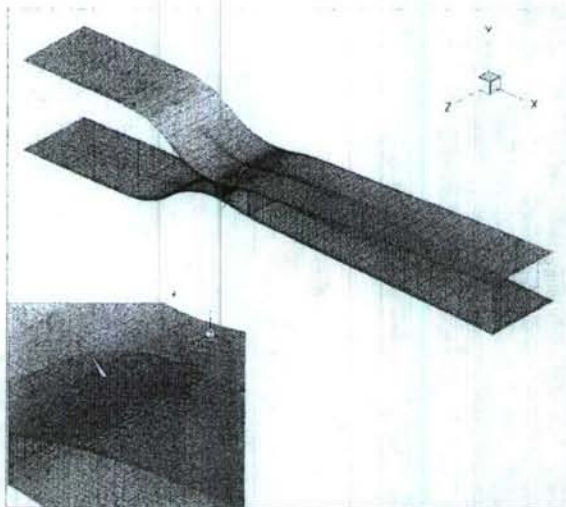
Figure 3. Computational grid used in 3-D Navier-Stokes simulation of the experiment hardware flowfield in Fig. 1. Grid resolution shown is $1/512^{th}$ of that used in the actual simulation.
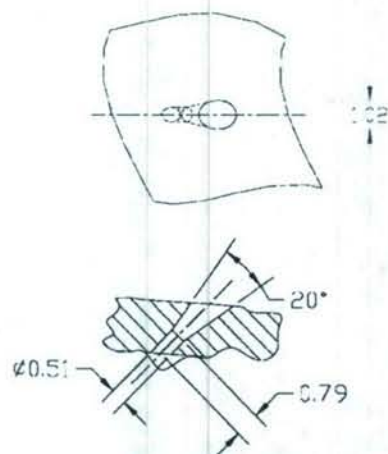
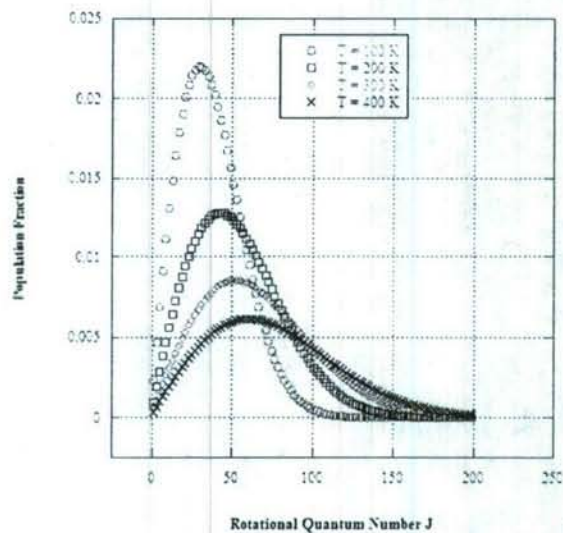Figure 2. Detailed drawing for the I_2 injector orifice used in the PLIF nozzle experiment hardware.

Figure 4. Variation of rotational population distribution for I_2 X, $\nu=0$, odd J versus temperature for the range of temperatures that exist within the data for the nozzle simulation.
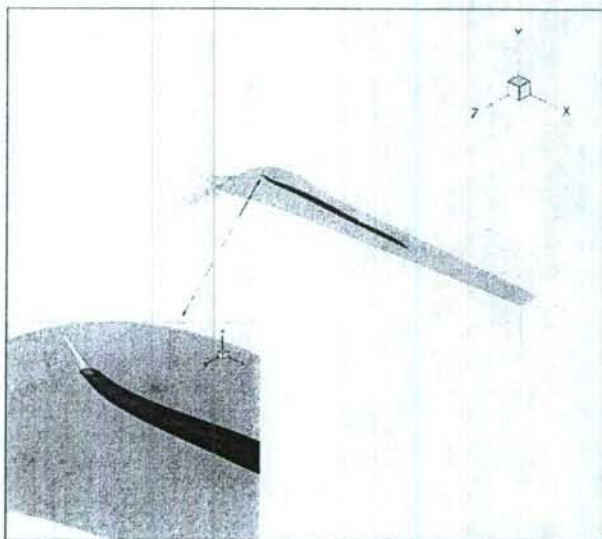
Figure 5. Isosurface plot for constant mole fraction of I_2, value $=4 \cdot 10^{-3}$, from the 3-D Navier-Stokes simulation of the PLIF nozzle experiment flowfield. The outline of the counter-rotating vortex pair is visible in the upper surface structure downstream of the orifice.
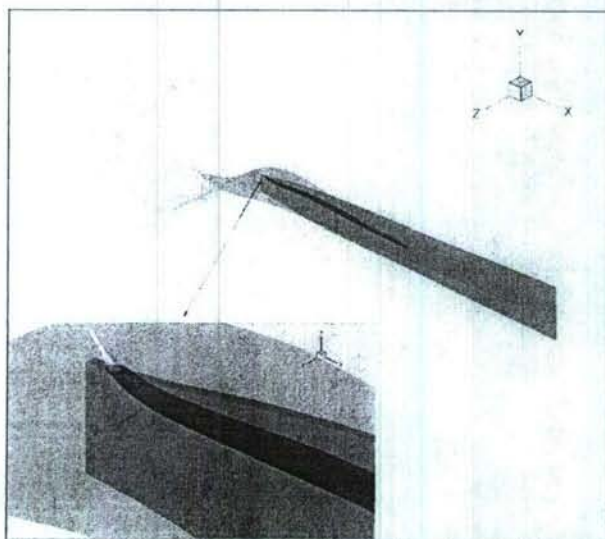
Figure 7. Illustration of 'sheet' sub-domain used for execution of the I_2 fluorescence model, in blue, with respect to the larger computational domain used in the 3-D Navier-Stokes simulation. Values are interpolated from the Navier-Stokes simulation domain to the 'sheet' domain.
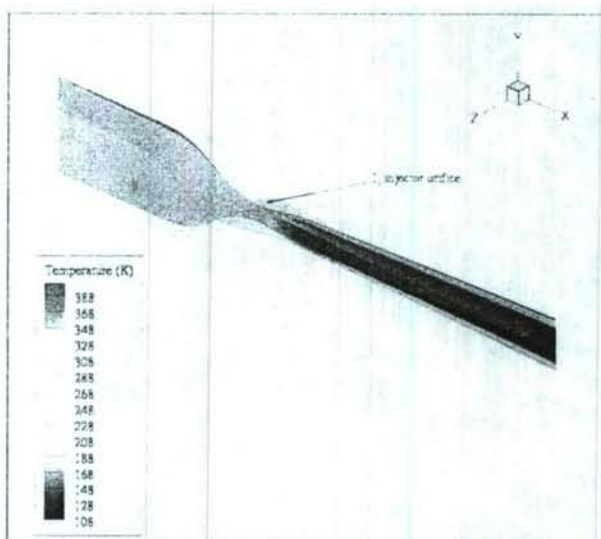
Figure 6. Temperature (K) contours within a 2-D planar cut through the center of the jet within the 3-D Navier-Stokes simulation of the PLIF nozzle experiment flowfield. Note that the jet fluid remains warmer than the surrounding fluid.
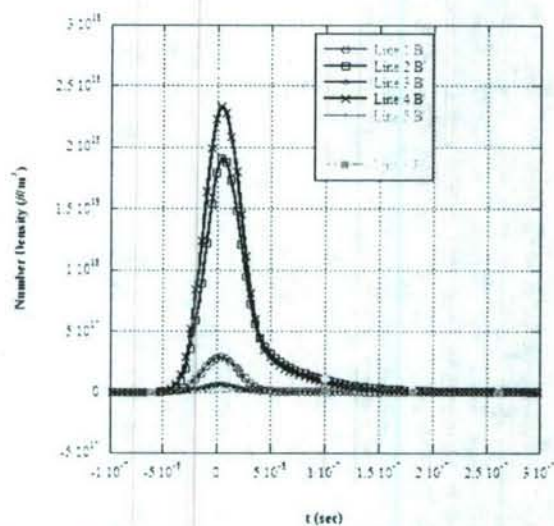
Figure 8. Predicted temporal variation of the B' states for a data point within the I_2 jet illustrating the variation in excitation during the laser pump from line to line.
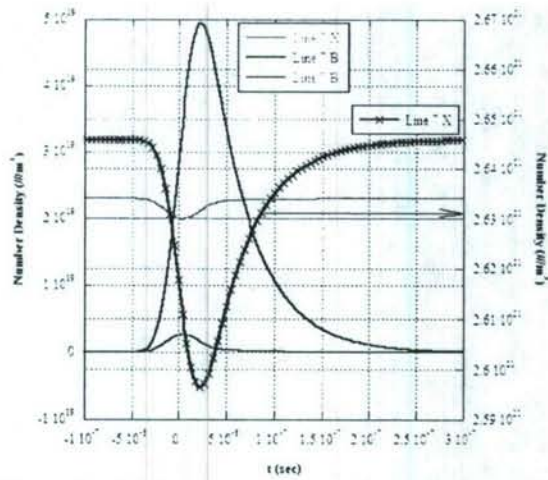
23

Figure 9. Predicted temporal variation of Line 7, $v''=1$, $J''=75$, $v'=21$, $J'=74$ from the I_2 fluorescence model. Note that the Y axis for the X states variable is to the right and that for the remaining variables is to the left.
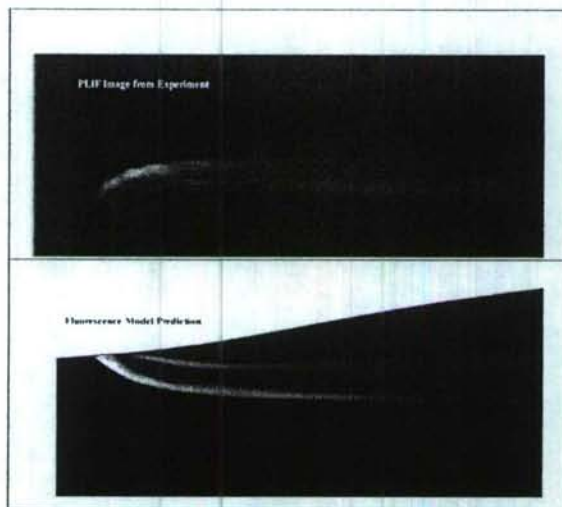

Figure 11. Comparison of experiment PLIF image with fluorescence model generated image within the streamwise laser sheet shown in Fig. 7
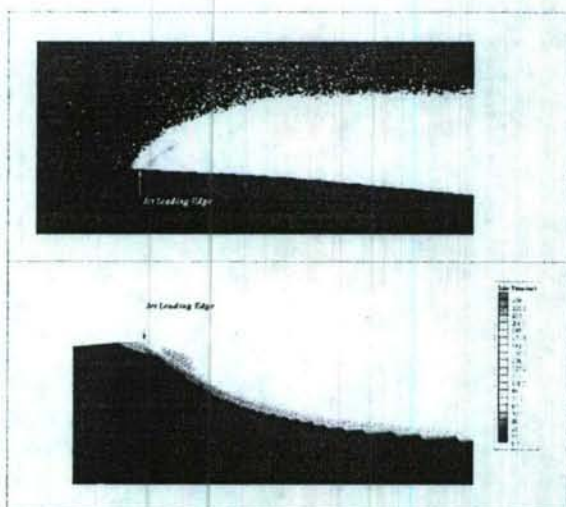
Figure 10. Comparison of the fluorescence lifetime as measured in the PLIF nozzle experiment, top image, with that from the fluorescence model. Note that the experiment includes reflection of the fluorescence light off of the nozzle wall.
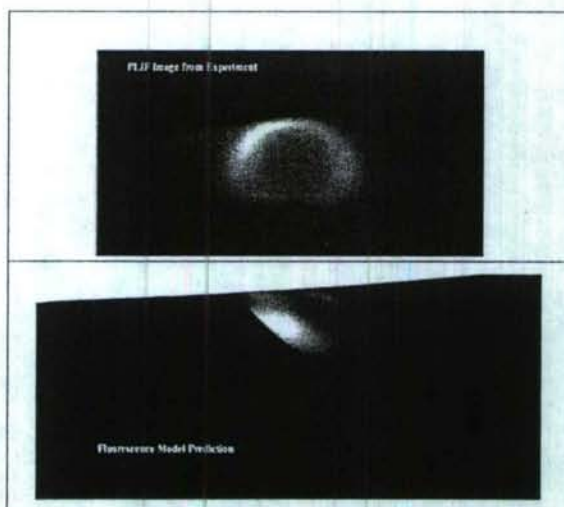

Figure 12. Comparison of experiment PLIF image with fluorescence model generated image within a sheet interrogating the flowfield at a 45° angle with respect to the flow axis at the trailing edge of the injector orifice. Note that the model generated image is integrally averaged across the width of the sheet.
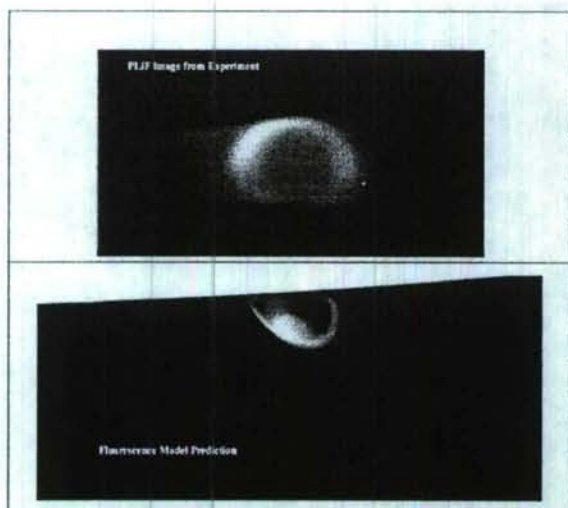
Figure 13. Comparison of experiment PLIF image with fluorescence model generated image within a sheet interrogating the flowfield at a 45° angle with respect to the flow axis at the trailing edge of the injector orifice. The model image is extracted from the plane at the center of the sheet, and does not include light contributions from the full thickness of the sheet.
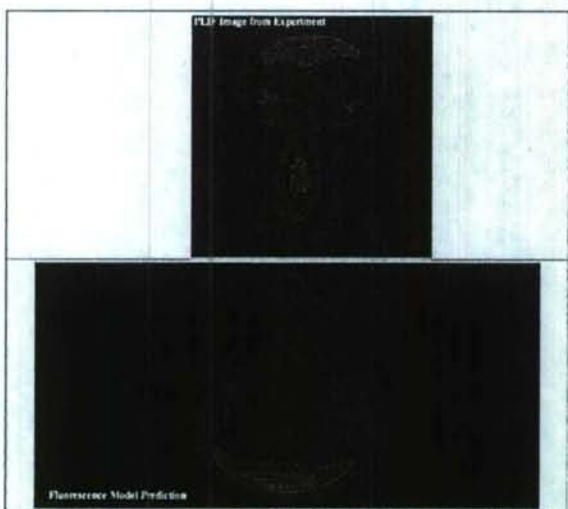

Figure 15. Comparison of experiment PLIF image with fluorescence model generated image within a sheet interrogating the flowfield at a 45° angle with respect to the flow axis 7 cm downstream of the injector orifice.
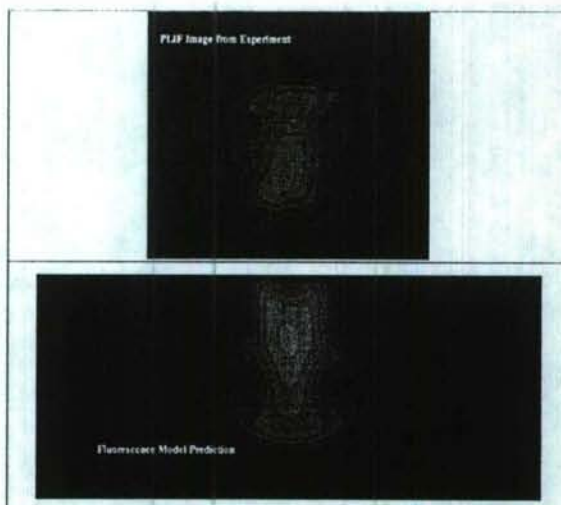
Figure 14. Comparison of experiment PLIF image with fluorescence model generated image within a sheet interrogating the flowfield at a 45° angle with respect to the flow axis 3 cm downstream of the injector orifice.

[1] Daily, J. W. and Chan, C., "Laser Induced Fluorescence Measurement of Sodium in Flames," *Sixth International Colloquium on Gasdynamics of Explosions and Reactive Systems*, Stockholm, Aug. 1977.

[2] Wrobel, N. H. and Pratt, N. H., "Laser Induced Sodium Fluorescence Measurements in a Turbulent Propane Diffusion Flame," *17th International Symposium on Combustion*, Leeds, 1978.

[3] Levy, D. H., Wharton, L., and Smalley, R. E., "Laser Spectroscopy in Supersonic Jets," *Chemical and Biochemical Applications of Lasers*, Academic Press, New York, 1977.

[4] Rapagnani, N. L. and Davis, S. J., "Laser-Induced I_2 Fluorescence Measurements in a Chemical Laser Flowfield," *AIAA Journal*, 17, No. 12, pp. 1402-1404, (1979.)

[5] McDaniel, J.C., "Investigation of laser-induced fluorescence for measurement of density in compressible flows," Ph.D. Dissertation, Department of Aeronautics and Astronautics, Stanford University, 1981.

[6] McDaniel, J.C., "Nonintrusive pressure measurements with laser-induced iodine fluorescence," in Combustion Diagnostics by Nonintrusive Methods, vol. 92 of the AIAA Progress in Aeronautics and Astronautics Series, T.D. McCay and J.A. Roux editors, pp. 107 131, American Institute of Aeronautics and Astronautics, Washington, (1984).

[7] Fletcher, D.G. and McDaniel, J.C. "Temperature measurement in a compressible flow field using laser-induced iodine fluorescence," *Optics Letters*, 12, no. 1, (1987).

[8] Hartfield, R., Rose, S., and Abbitt, J. "Computational fluid imaging for iodine fluorescence in compressible flows," *Applied Mathematics and Computation*, 95, pp. 63-73, (1998).

[9] N. L. Rapagnani and S. L. Davis, "Laser Induced Fluorescence: A Diagnostic for Fluid Mechanics", *Lasers and Applications*, 5, pp. 127, (1985).

[10] Rapagnani, N. L. and Zumpano, F. R., "Theoretical and Experimental Description for a Radial Supersonic Flowfield," *AIAA Journal*, 24, No. 11, pp. 1758-1765, (1986).

[11] Noren, C. A., Rothschopf, G., Perschbacher, T., Madden, T. J., Hager, G. D., Truman, C. R., Vorobieff, P. V., "PLIF Flow Visualization of a Supersonic Injection COIL Nozzle," AIAA Paper 2005-5388, *36th Plasmadynamics and Lasers Conference*, Toronto, Ontario, June 6-9, 2005.

[12] Noren, C.A., Truman, R.C., Vorobieff, P.V., Madden, T.J., and Hager, G.D. "PLIF Visualization and Quantitative Mixing Measurements of a Supersonic Injection Nozzle," AIAA-2006-2895, *37th AIAA Plasmadynamics and Lasers Conference*, San Francisco, CA, June 5-8, 2006.

[13] Ramshaw, J. D. and Dukowicz, J. K., "APACHE: A Generalized Mesh Eulerian Computer Code for Multicomponent Chemically Reactive Fluid Flow," Los Alamos Report LA-7427, Jan. 1979.

[14] Azyazov, V.N. and Heaven, M. C., work in progress.

[15] Tellinghuisen, J., "Intensity factors for the I_2 B $\rightarrow$ X band system," *Journal of Quantum Spectroscopy and Radiative Transfer*, **19**, pp. 149 161, (1972).

[16] Broyer, M., Vigué, J., and Lehmann, J.C., "Direct evidence of the natural predissociation of the I_2 B state through systematic measurement of lifetimes," *Journal of Chemical Physics*, **63**, No. 12, pp. 5428-5431, (1975).

[17] Vigué, J., Broyer, M., and Lehmann, J.C., "Quantum interference effect between the magnetic and natural predissociations in the $B^3 \Pi_{0+u}$ state of I_2. A new experimental proof," *Journal of Physics B: Atomic and Molecular Physics*, **7**, pp. L158-L161, (1974).

[18] Cappelle, G. A. and Broida, H. P. "Lifetimes and quenching cross sections of $I_2(B)$" *J. Chem. Phys.* **58**, 4212 (1973)

[19] W. G. Lawrence, T. A. Van Marter, M. L. Nowlin, and M. C. Heaven, "Inelastic collision dynamics of vibrationally excited $I_2(X)$" *J. Chem. Phys.* **106**, 127 (1997)